



HAL
open science

Thermal characterization of polyethylene glycol 600 in liquid, solid phases and through the phase transition

Justine Noel, Yves Jannot, Christel Métivier, Nicolò R Sgreva

► **To cite this version:**

Justine Noel, Yves Jannot, Christel Métivier, Nicolò R Sgreva. Thermal characterization of polyethylene glycol 600 in liquid, solid phases and through the phase transition. 2021. hal-03516867v4

HAL Id: hal-03516867

<https://hal.science/hal-03516867v4>

Preprint submitted on 21 Jul 2022 (v4), last revised 29 Sep 2022 (v5)

HAL is a multi-disciplinary open access archive for the deposit and dissemination of scientific research documents, whether they are published or not. The documents may come from teaching and research institutions in France or abroad, or from public or private research centers.

L'archive ouverte pluridisciplinaire **HAL**, est destinée au dépôt et à la diffusion de documents scientifiques de niveau recherche, publiés ou non, émanant des établissements d'enseignement et de recherche français ou étrangers, des laboratoires publics ou privés.

Thermal characterization of polyethylene glycol 600 in liquid and solid phase and across the phase transition

Justine Noel^a, Yves Jannot^a, Christel Métivier^{a,*}, Nicolò R. Sgreva^a

^a*Université de Lorraine, LEMTA, CNRS, 54000 Nancy, France.*

Abstract

The polyethylene glycol (PEG) is characterized by experimental means in both solid and liquid phase. Main thermal properties inherent to the phase transition are also provided. More specifically, we focus on PEG 600, whose average molar mass is 600 g mol^{-1} and melting temperature transition is around 283-298 K. The phase change does not occur at a given temperature but rather over a range of temperature, highlighting the complexity of the material. Several methodologies have been developed and calibrated in order to obtain, in both phases, the density and the thermal conductivity. A temperature dependence fit is proposed for the density in liquid phase. The relative density variation from the liquid to solid phase is significant as it can reach about 35 %, meaning a quite large volume shrinkage. Differential Scanning Calorimetry (DSC) has been used for measuring the heat capacity of solid and liquid phase and the effective heat capacity at the transition states. The latent heat of fusion and solidification converge to a value of around 128 kJ kg^{-1} . Undercooling effects are mitigated by performing DSC with slow temperature variation rates. Lastly, we have also observed several exothermic peaks during the solidification process that are related to structural reorganizations of the material.

1. Introduction

2 Polyethylene glycol (PEG) is a polyether present in our daily life and its
3 employment covers a wide range of industries, such as cosmetics, pharma-
4 ceuticals, food manufacturing, inks. As an example, it is used as a thickener

*christel.metivier@univ-lorraine.fr

5 agent in cosmetic products (liquid soaps, moisturizers, shampoos, etc.) and
6 paramedical products (hydro-alcoholic gels, intimate lubricants [1], etc.). It
7 is also used as a solvent in printer inks or to manufacture paint balls, as a
8 food additive and in certain polyester resins. Because it is a bio-compatible
9 product [2], it is also widely used in medical treatments and vaccines [3], as
10 recently for Covid-19 vaccine. In addition, the polyethylene glycol presents
11 remarkable properties: from a chemical viewpoint it is stable, non corro-
12 sive and non toxic. Another significant advantage lies in the large variety
13 of temperatures at which the solid/liquid transition occurs. Depending on
14 PEG's molecular weight, phase transition occurs for instance around 283-
15 293 K for PEG 600, 321-323 K for PEG 1000 [4] and around 324 K for PEG
16 1500 [5]. For these reasons, numerous studies have been devoted to propose
17 Composite Phase Change Materials (CPCMs) based on polyethylene glycol
18 [6, 7, 8, 9, 10, 11, 12]. Phase change materials (PCMs) are widely studied
19 in the field of energy storage/release since a large amount of energy can be
20 transferred during the phase change via latent heat. Energy is stored during
21 endothermic transformations (e.g. solid to liquid) while it is released dur-
22 ing exothermic transformations. The large latent heat of PEG makes it a
23 very interesting and attractive PCM. Furthermore, it matches perfectly the
24 criteria related to the choice of PCMs, such as being low-cost, non-toxic,
25 non-flammable, non-corrosive and biodegradable (bio-compatible), i.e. eco-
26 friendly. The uses of PEG in Composite PCMs can concern thermal reg-
27 ulation in buildings [13] or pavements [8] as well as in photovoltaic panels
28 [4, 12].

29 Despite the wide use of PEG, only few papers were devoted to characterize
30 the thermal properties of polyethylene glycol alone. Recently, Kou et al. [14]
31 have measured heat capacities of PEG for molar mass varying from 2000 to
32 20 000 g mol⁻¹. For smaller molar mass, as it is the case of PEG 600 (average
33 molar mass of 600 g mol⁻¹), available data correspond mainly to properties
34 for the liquid phase only. For instance, density measurements are provided
35 by several authors [15, 16, 17, 18], but they are given only for the liquid phase
36 for few temperature values, not sufficient to obtain the thermal expansion
37 coefficient. Some properties of PEG 600 are also given by Lane [19] who
38 focuses on properties of several PCMs. For PEG 600, the author indicates
39 the latent heat of melting and only one value for the melting temperature.
40 Lane [19] also provides the thermal conductivity and the density in liquid
41 phase for a couple of temperature values. Only a few other studies present
42 the thermal conductivity of liquid phase, e.g. [17, 19]. Thus, properties of

43 PEG remain partially and scatteredly described in the literature. Moreover,
44 this small number of measured properties is obtained only for the liquid
45 phase. To our knowledge, the latent heat of solidification, the freezing point,
46 the thermal conductivity, the density and the heat capacity for the solid
47 phase are not available in the literature.

48 From a structural viewpoint, PEG's properties - in particular at the
49 solid/liquid transition - depend not only on the molecular weight but also
50 on the protocols involved in measuring them. Several types of aggregate
51 structures, such as helical or spherical conformations have been observed
52 within the freezing process [20, 21]. Understanding the correlation between
53 structural modifications and imposed experimental conditions is crucial since
54 the structural organization can have a significant impact on the macroscopic
55 properties. Indeed, in the case of semi-crystalline polymers as it is for PEG,
56 Bogdanov et al. [22] highlighted the influence of the cooling rate on the
57 exothermic crystallization peak by means of isothermal Differential Scan-
58 ning Calorimetry (DSC). Furthermore, a correlation between the heat flux
59 measured by DSC and the degree of crystallinity of PEG is proposed by
60 Pielichowski & Flejtuch [23].

61 As a first step in the understanding of the relationships between PEG's
62 behaviour and conditions of use, we clarify and provide new macroscopic
63 properties for PEG 600. The aim of our study is to characterize this polyether
64 in both the solid and liquid phase. In the liquid phase, we provide original
65 values of macroscopic properties and how they vary with temperature. In the
66 solid phase, we aim to fill the data gap in the literature. We carefully detail
67 the methodologies and protocols used to obtain the main thermal properties
68 in each phase (density, effective heat capacity and thermal conductivity) and
69 the latent heat of melting and solidification. In section 2, the different mea-
70 surement techniques and protocols used are detailed. Results are provided
71 in section 3 where they are also compared with the available literature. The
72 paper ends with conclusions and perspectives.

73 **2. Methods and experimental devices**

74 *2.1. Material*

75 Polyethylene glycol (PEG) is a linear polyether made from ethylene gly-
76 col monomers characterized by a molar mass generally smaller than 20 000
77 g mol^{-1} . In this study, we aim to characterize the polyethylene glycol with

78 molar mass of around 600 g mol^{-1} , named PEG 600 (Table 1). The sam-
79 ples of PEG 600 that we used were purchased in synthesis grade from Merck
80 (CAS 25322-68-3, labeled average molecular mass of 570-630) and were used
81 as received, i.e. without further purification. Several batches have been used
82 to verify reproducibility of results.

83 The temperature of the solid-liquid phase change is indicated by the sup-
84 plier within the range of 290.15-293.15 K.

85 The initial degree of purity of the material is not stated in the product
86 specifications provided by the manufacturer and has not been subsequently
87 measured. However, [18] report an initial purity of $\geq 99.8\%$ for PEG 600
88 provided by the same manufacturer as our (same CAS number). No purifi-
89 cation method was used in [18]. For this reason, and considering the good
90 agreement we have obtained in thermophysical properties with available lit-
91 erature (see next section 3), no further purification was performed on our
92 PEG samples.

93 The water content (w) in our samples is estimated by taking the weight
94 of PEG samples before and after drying them at 353.15 K for 24 hours (see
95 supplementary materials). We have found a water content of 0.24 %, with a
96 combined expanded uncertainty $U_c(w) = 0.02 \%$ with 0.95 level of confidence
97 (coverage factor $k=2$).

98 In Table 1 we also report the samples of water and glycerol employed
99 during methods validation. We used ultra-pure water (Anton Paar) to verify
100 density measurements obtained with the densimeter. We used glycerol for
101 the validation of the transient hot needle method used to estimate thermal
102 conductivity. For the validation of other analysis methods we used deminer-
103 alized water. The latter is produced by a reverse osmosis unit from Ondeo
104 (Purite Select A640/GP, 1-10 $\text{M}\Omega \text{ cm}$). To ensure good water quality, filter
105 cartridges are changed before the water resistance drops to 1 $\text{M}\Omega \text{ cm}$. We
106 underline that the water resistance is given directly by the device when it is
107 produced.

108

109 *2.2. Density*

110 *2.2.1. Liquid phase*

111 The density (ρ) of PEG 600 in liquid phase is measured by using a den-
112 simeter DMA 5000M, Anton Paar. The densimeter provides a $10^{-6} \text{ g cm}^{-3}$

Table 1: Samples table

Chemical Name	Source	Initial Mass Fraction Purity, x_e	Purification Method ^b
Polyethylene Glycol 600	Merck CAS 25322-68-3	99.8 % ^a	none
Ultra-pure water	Anton Paar	-	none
Demineralized water	Tap water	-	reverse osmosis
Glycerol	Fisher Chemical CAS 56-81-5	99 %	none

^aValue from [18].

^bfurther purification in addition to that of the supplier ('Source')

113 accuracy in the temperature range of 273.15-333.15 K, while for larger tem-
 114 peratures (up to a maximum of 373.15 K) the accuracy decreases to 10^{-4}
 115 g cm^{-3} . The precision on the temperature is 0.01 K. Calibration and valida-
 116 tion of the device are given in the supplementary material. Density measure-
 117 ments are carried out at constant pressure P (atmospheric pressure) and at
 118 different temperature values within the range of 294.15-373.15 K where PEG
 119 600 is liquid. Isothermal conditions are obtained by imposing temperature
 120 steps with a 1 K increment in the range 294.15-323.15 K, followed by a 5 K
 121 increment up to the temperature of 373.15 K. In the liquid phase, the time
 122 to achieve the thermal stability is about 5 minutes per temperature step.

123 To ensure reproducible results, density is measured on three different
 124 samples (volume of ~ 1 mL) from two different batches. At a given temper-
 125 ature, the maximal variation between measurements is found to be 2×10^{-5}
 126 g cm^{-3} . The final value of density is taken as the mean of these measure-
 127 ments. From the temperature dependence of the density, we evaluate the
 128 thermal expansion coefficient β as follows

$$\beta = -\frac{1}{\rho_{ref}} \left(\frac{\partial \rho}{\partial T} \right)_P, \quad (1)$$

129 with $\rho_{ref} = \rho(T_{ref})$ being a reference density defined at the temperature T_{ref} .
 130 The thermal expansion coefficient indicates the first-order density variations
 131 with temperature (Boussinesq approximation) at constant pressure [24] and,
 132 for a given mass of a material, it also corresponds to the volume variation
 133 with temperature.

Table 2: Pressure measurements performed for the pycnometer calibration at 273.75 K - Steps (1) and (2). P_i is the initial pressure and P_f the final pressure ^a.

Step (1)			Step (2)		
P_i (bar)	P_f (bar)	P_f/P_i	P_i (bar)	P_f (bar)	P_f/P_i
3.654	1.685	46.1 %	3.655	2.002	54.7 %
3.660	1.696	46.3 %	3.650	2.002	54.8 %
3.665	1.706	46.5 %	3.603	1.976	54.8 %

^aStandard uncertainties u are $u(P) = 0.001$ bar and $u(T) = 0.01$ K.

134 *2.2.2. Solid phase*

135 The density of PEG 600 in solid phase is achieved using a lab-made
 136 pycnometer. The device is placed in a thermostatic enclosure BinderTM
 137 KBF 115 in order to control the temperature. The temperature set in the
 138 binder is 273.75 K in order to ensure that our PEG sample will be fully
 139 solid. The pycnometer consists in two different cavities of volume V and V'
 140 separated by a valve, as represented in Fig. 1. The measurement procedure
 141 is to initially obtain the vacuum in both cavities, i.e. $P' = P = 0$, then close
 142 the valve and impose a pressure P_i to the lower cavity. The valve is then
 143 opened involving pressure variations until an equilibrium is reached within
 144 the two cavities, leading to a final pressure P_f . The pressure is measured
 145 using a Mano 2000 Leo 3 Keller with an accuracy of 1 mbar.

146 We first start by a calibration of the device, i.e. we determine the volumes
 147 V and V' of each cavity by repeating several times the above mentioned
 148 procedure through Steps (1) and (2), as indicated in Fig. 1 b. Volumes V
 149 and V' are determined via the following equation

$$P_i V = P_f \times (V + V' - V_{ref}), \quad (2)$$

150 where V_{ref} corresponds to the volume of a cylinder of height 0.02 m and
 151 radius 0.04 m. The procedure is repeated three times. Measurements are
 152 summarized in Table 2. The precision of the method has been evaluated by
 153 performing step (3) using a calibrated volume of solid. Details are provided
 154 in the supplementary material.

155 Finally, Step (3) is performed with a given mass of PEG (Fig. 1 b). The
 156 volume of solid PEG is obtained using eq. (2) in which V_{ref} is replaced by
 157 the unknown sample volume. The density of PEG in solid phase is deduced
 158 from this measurement.

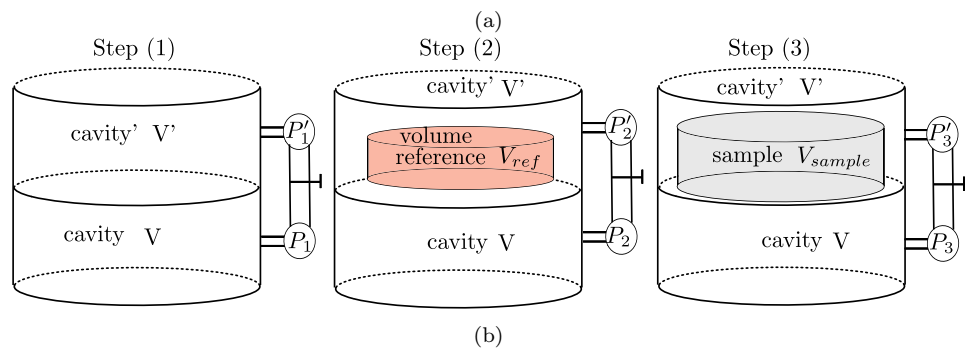


Figure 1: (a) Photo of the pycnometer. (b) Sketch of the set-up for calibration - Step (1) and Step (2) - and for measuring the density of solid PEG 600 - Step (3) -.

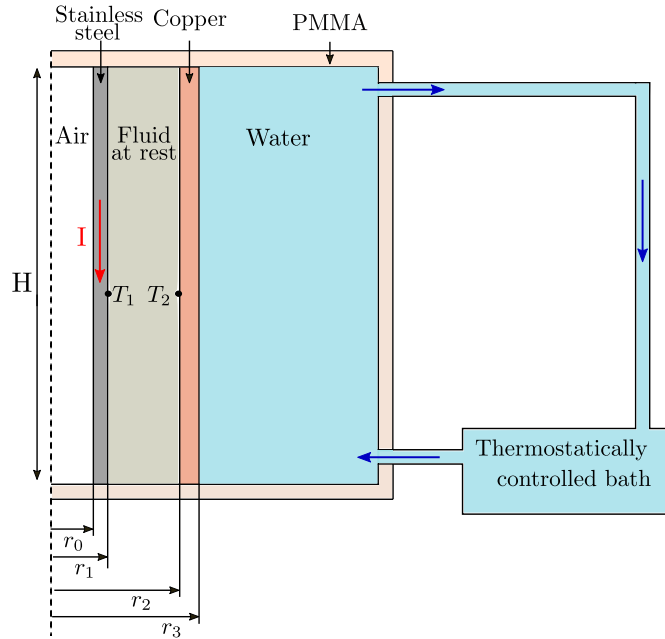


Figure 2: Sketch of the hot tube device used for thermal conductivity measurements. $r_0 = 2.54$ mm, $r_1 = 2.75$ mm, $r_2 = 6.00$ mm

159 *2.3. Thermal conductivity*

160 *2.3.1. Liquid phase*

The thermal conductivity of the liquid phase is measured via the stationary hot tube method [25, 26]. A sketch of the device developed in our laboratory is shown in Fig. 2. A validation of the device with demineralized water is provided in the supplementary material. The sample is introduced in liquid phase into the gap between two coaxial cylinders made of copper (the outer one) and stainless steel (the inner one). We ensure that the sample fills completely the space between the two cylinders, i.e. the space between r_1 and r_2 in Fig. 2. An electric current I is applied to the inner cylinder, producing heat flux by Joule effect. The outer part of the copper cylinder is maintained at a given temperature via a temperature controlled water flow. The temperatures T_1 and T_2 are measured using two type K thermocouples locked on the wall of the cylinders, i.e. at the boundaries of the liquid layer (as indicated in Fig. 2). Moreover, in order to avoid any up-down wall effects, thermocouples are located at the mid-height of the device. The temperature difference is measured thanks to the voltage difference U between these two

thermocouples:

$$\Delta T = T_1 - T_2 = U/k,$$

161 where k is a constant equal to $k = (39.2 + 0.064 \times T_2 - 0.005 \times T_2^2) \times 10^{-6}$
 162 V K^{-1} . Thermocouples are connected to a cold junction block. Tension and
 163 electrical current are measured with a Keysight U3401A and an ISO-TECH
 164 IDM91E multimeter, respectively.

165 For a purely conductive regime in the liquid layer (fluid at rest), the
 166 thermal conductivity can be deduced as follows [25]:

$$\lambda = \frac{\rho_{el} I^2 \ln(r_2/r_1)}{2\pi^2(r_1^2 - r_0^2)\Delta T} \quad (3)$$

167 with $\rho_{el} = 7.3 \times 10^{-7}(1 + 1.36 \times 10^{-2}(T - T_{ref})) \Omega \text{m}$ being the electrical
 168 resistivity of the stainless steel and T_{ref} a temperature reference equal to
 169 293.15 K.

170 The dimensions of the device are determined under the condition that no
 171 convection occurs for a wide range of fluids. According to [27], we ensure
 172 that the following condition is satisfied:

$$\frac{Ra}{H^+} < 400 \quad (4)$$

173 where $H^+ = H/\delta$, H is the height of the cylinders, $\delta = r_2 - r_1$ is the thickness
 174 of the liquid layer and Ra corresponds to the Rayleigh number given by

$$Ra = \frac{\rho g \beta \Delta T \delta^3}{\mu a}, \quad (5)$$

175 with μ being the dynamic viscosity and a the thermal diffusivity of the
 176 fluid.

177 This condition is verified a posteriori and in the case of our measurements
 178 with PEG we estimate $Ra/H^+ \approx 15 - 20 \ll 400$.

179 Device validation performed with demineralized water leads to a maximal
 180 difference in thermal conductivity of 2.5 % with values provided by Ramires
 181 *et al.* [28], i.e. a variation of $0.02 \text{ W m}^{-1} \text{ K}^{-1}$ (see supplementary material).
 182 Since the device is filled by the PCM in liquid phase, the volume of the sample
 183 varies with the temperature with a maximal variation occurring during the
 184 phase transition. As it is with most materials, PEG decreases in volume from
 185 liquid to solid phase. This can lead to imperfect contacts at walls during the

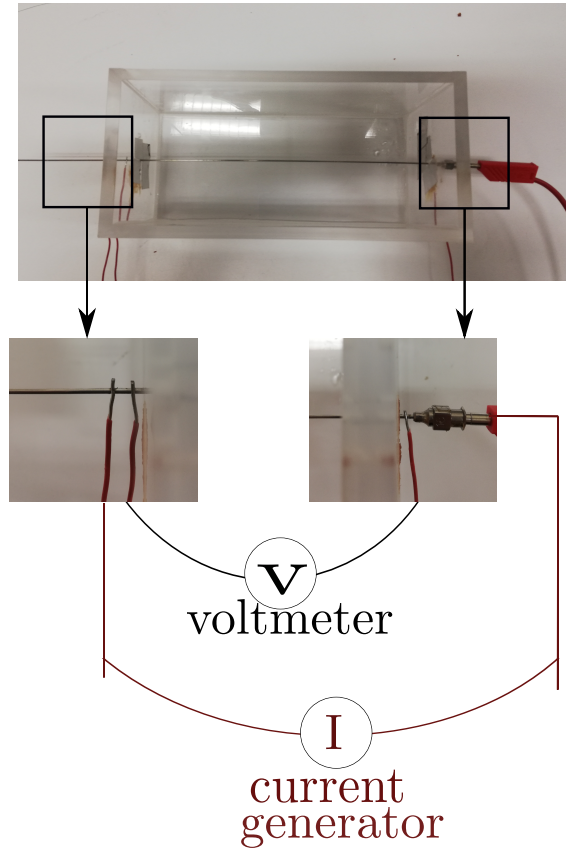


Figure 3: Photo of the heated needle device

186 solidification, as detailed in Appendix A. In this case, i.e. when thermal
 187 contact resistances are present at walls, the device becomes unsuitable for
 188 measuring thermal conductivity of materials in solid phase. For this reason,
 189 we propose another technique to carry out measurements in the solid phase.
 190 This technique is detailed in the following paragraph.

191 *2.3.2. Hot needle method*

192 We developed a specific device in order to measure the thermal con-
 193 ductivity of materials in solid or liquid phase. The device consists in a
 194 $200 \times 120 \times 120 \text{ mm}^3$ cavity made of PMMA that is filled with the sample.

195 A stainless steel hollow needle of length 300 mm is placed at the center
 196 of the device (Fig. 3). Needle's inner and outer radii are $r_i = 0.80 \text{ mm}$ and
 197 $r_e = 1.25 \text{ mm}$, respectively. The needle is heated by Joule effect and the

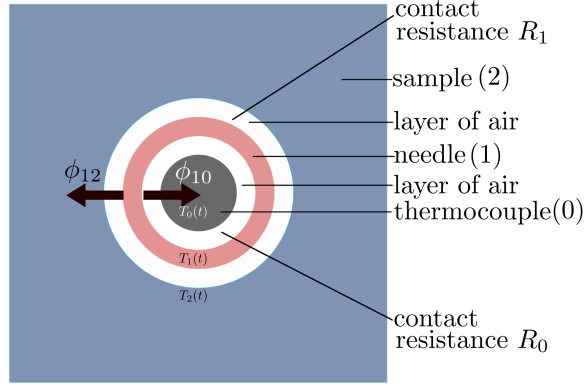


Figure 4: Schematic cross section of the hollow needle probe. The subscripts “0”, “1” and “2” refer to the thermocouple, the needle and the sample, respectively.

198 corresponding heat flow rate per unit of length L is $\phi = (UI)/L$, with U the
 199 electrical tension and I the electric intensity. Temperature is measured at the
 200 central point inside the needle with a K-type sheath thermocouple of radius
 201 $r_t = 0.5$ mm. Electrical tension and current are measured with a Tektronix
 202 DMM and an ISO-TECH IDM91E multimeter, respectively. Temperatures
 203 are recorded using a TC-08 Picolog device with a frequency of 10 Hz.

204 According to Fig. 4, in the following description we use the subscripts
 205 “0”, “1” and “2” to refer to the thermocouple, the needle and the sample,
 206 respectively.

207 The device is placed in a BinderTM KBF 115 thermostatic chamber in
 208 order to maintain the system at a controlled temperature. The thermostatic
 209 chamber also guarantee a constant initial temperature $T(t = 0)$ in the whole
 210 system, i.e. $T_0(0) = T_1(0) = T_2(0)$, being the initial temperature of the
 211 thermocouple, the needle and the sample, respectively. We assume uniform
 212 temperature field in the needle, $T_1(t)$, and in the thermocouple, $T_0(t)$, since
 213 they are very thin. Moreover, since contacts at interface 1-2, i.e. needle-
 214 sample, and at the interface 1-0, i.e. needle-thermocouple, are not perfect,
 215 also the thermal contact resistances R_1 and R_0 (see Fig. 4) have to be taken
 216 into account. Finally, due to the long length of the cavity, we consider an
 217 unidirectional dependence of parameters at the center of the cavity.

218 As the needle is heated, the total heat flow rate ϕ due to Joule effect can
 219 be split in two components, i.e. $\phi = \phi_{10} + \phi_{12}$ where ϕ_{12} is the heat transferred
 220 to the material and ϕ_{10} the heat transferred to the thermocouple. Heating
 221 the needle also induces transient variations in temperature within the whole

222 system. Thermal properties of PEG can be obtained by considering the
 223 heat equation (conductive regime) in two domains assorted with boundary
 224 conditions. For this purpose, we use the quadrupole formalism proposed by
 225 Maillet *et al.* [29].

226 The first domain is bounded by the outer surface of the needle ($r_1 = r_e (\approx$
 227 $r_i)$) and a surface of the material sample ($r_2 \rightarrow \infty$). Following the method
 228 proposed by Maillet *et al.* [29], the thermal quadrupole formalism writes:

$$\begin{bmatrix} \theta_1 \\ \Phi_{12} \end{bmatrix} = [M1][M2] \begin{bmatrix} \theta_2 \\ \frac{\theta_2}{Z} \end{bmatrix} = \begin{bmatrix} 1 & 0 \\ C_1 p & 1 \end{bmatrix} \begin{bmatrix} 1 & R_1 \\ 0 & 1 \end{bmatrix} \begin{bmatrix} \theta_2 \\ \frac{\theta_2}{Z} \end{bmatrix} = \begin{bmatrix} 1 & R_1 \\ C_1 p & 1 + R_1 C_1 p \end{bmatrix} \begin{bmatrix} \theta_2 \\ \frac{\theta_2}{Z} \end{bmatrix} \quad (6)$$

with:

$\theta_1 = \mathcal{L}(T_1(t) - T_1(0))$ being the Laplace transform of the temperature varia-
 tion in the needle, i.e. $T_1(t) - T_1(0)$,

$\theta_2 = \mathcal{L}(T_2(t) - T_2(0))$ the Laplace transform of the temperature variation in
 the sample at the interface needle-material, i.e. $T_2(t) - T_2(0)$,

$\Phi_{12} = \mathcal{L}(\phi_{12})$ the Laplace transform of ϕ_{12} ,

$M1$ the quadrupolar matrix representing the needle as a pure capacity C_1 ,

$M2$ the quadrupolar matrix representing the contact resistance at the inter-
 face 1-2,

p the Laplace parameter (s^{-1}),

R_1 the thermal contact resistance per unit of length at the interface 1-2
 (m K W^{-1}), and

$$C_1 = \pi(r_e^2 - r_i^2)\rho_1 c_1, \quad (7)$$

$$Z = \frac{K_0(qr_e)}{2\pi\lambda q r_e K_1(qr_e)}, \quad (8)$$

$$q = \sqrt{\frac{p}{a}} \quad (9)$$

229 where ρ_1 is the density of the needle (kg m^{-3}), c_1 the specific heat of the
 230 needle ($\text{J K}^{-1} \text{kg}^{-1}$), a the thermal diffusivity of the sample ($\text{m}^2 \text{s}^{-1}$), and λ
 231 the thermal conductivity of the sample ($\text{W m}^{-1} \text{K}^{-1}$).

232 Similarly, we consider a second domain that is bounded by the thermocou-
 233 ple $r_0 = 0 (\approx r_i)$ and the inner needle surface $r_1 = r_i (\approx r_e)$. The quadrupole
 234 formalism leads to:

$$\begin{bmatrix} \theta_1 \\ \Phi_{10} \end{bmatrix} = [M3][M4] \begin{bmatrix} \theta_0 \\ 0 \end{bmatrix} = \begin{bmatrix} 1 & R_0 \\ 0 & 1 \end{bmatrix} \begin{bmatrix} 1 & 0 \\ C_0 p & 1 \end{bmatrix} \begin{bmatrix} \theta_0 \\ 0 \end{bmatrix} = \begin{bmatrix} 1 + R_0 C_0 p & R_0 \\ C_0 p & 1 \end{bmatrix} \begin{bmatrix} \theta_0 \\ 0 \end{bmatrix} \quad (10)$$

235 with:

236 $\theta_0 = \mathcal{L}(T_0(t) - T_0(0))$ being the Laplace transform of the thermocouple's
237 temperature variation, i.e. $T_0(t) - T_0(0)$,

238 $\Phi_{10} = \mathcal{L}(\phi_{10})$ the Laplace transform of the heat flow rate ϕ_{10} ,

239 $M3$ the quadrupolar matrix representing the contact resistance at the inter-
240 face 0-1,

241 $M4$ the quadrupolar matrix representing the thermocouple as a pure capac-
242 ity C_0 ,

243 R_0 the thermal contact resistance per unit length between the thermocouple
244 and the needle (m K W^{-1}), and

245

$$C_0 = \pi r_t^2 \rho_0 c_0, \quad (11)$$

246 where ρ_0 is the density of the thermocouple (kg m^{-3}) and c_0 the specific heat
247 of the thermocouple ($\text{J K}^{-1} \text{kg}^{-1}$).

From Eq.(6) we deduce:

$$\theta_1 = \left(1 + \frac{R_1}{Z}\right) \theta_2, \quad (12)$$

$$\Phi_{12} = \left(C_1 p + \frac{1 + R_1 C_1 p}{Z}\right) \theta_2 = \left(C_1 p + \frac{1 + R_1 C_1 p}{Z}\right) \frac{\theta_1}{1 + \frac{R_1}{Z}}. \quad (13)$$

From Eq.(10) we deduce:

$$\theta_1 = (1 + R_0 C_0 p) \theta_0, \quad (14)$$

$$\Phi_{10} = C_0 p \theta_0 = \frac{C_0 p}{1 + R_0 C_0 p} \theta_1. \quad (15)$$

The Laplace transform of the total heat flow rate ϕ writes:

$$\mathcal{L}(\phi) = \frac{\phi}{p} = \Phi_{12} + \Phi_{10} = \left(\frac{Z C_1 p + 1 + R_1 C_1 p}{Z + R_1} + \frac{C_0 p}{1 + R_0 C_0 p}\right) \theta_1, \quad (16)$$

and by substituting Eq.(14) into Eq.(16) we obtain

$$\theta_0 = \frac{\phi}{p} \frac{Z + R_1}{(Z + R_1)[(C_0 + C_1)p + R_0 C_0 C_1 p^2] + 1 + R_0 C_0 p}. \quad (17)$$

At long time ($p \rightarrow 0$), the above equations simplify to:

$$\theta_0 = \frac{\phi}{p}(Z + R_1), \quad (18)$$

$$K_0(qr_e) = -\ln\left(\frac{qr_e}{2}\right) - \gamma, \quad (19)$$

$$K_1(qr_e) = \frac{1}{qr_e}, \quad (20)$$

$$\theta_0(p) = \frac{\phi}{p} \left[-\frac{\ln\left(\frac{qr_e}{2}\right)}{2\pi\lambda} - \frac{\gamma}{2\pi\lambda} + R_1 \right] = \quad (21)$$

$$= \frac{\phi}{p} \left[-\frac{\ln(p)}{4\pi\lambda} - \frac{\ln\left(\frac{r_e}{2\sqrt{a}}\right)}{2\pi\lambda} - \frac{\gamma}{2\pi\lambda} + R_1 \right]. \quad (22)$$

By performing the inverse Laplace transform, we obtain:

$$T_0(t) = \phi \left[\frac{\ln(t)}{4\pi\lambda} + \frac{\gamma}{4\pi\lambda} - \frac{\ln\left(\frac{r_e}{2\sqrt{a}}\right)}{2\pi\lambda} - \frac{\gamma}{2\pi\lambda} + R_1 \right], \quad (23)$$

and finally

$$T_0(t) = \frac{\phi}{4\pi\lambda} \ln(t) + \phi \left(\frac{-\gamma}{4\pi\lambda} - \frac{\ln\left(\frac{r_e}{2\sqrt{a}}\right)}{2\pi\lambda} + R_1 \right). \quad (24)$$

248 Equation (24) highlights a logarithm dependence of T_0 with time that
 249 becomes the dominant term at long time. This equation is valid only if the
 250 regime remains conductive and the medium is infinite. Hence, we can write:

$$T_0(t) = D_1 + D_2 \times \ln(t) \quad (25)$$

251 with D_1 and D_2 being two constants which depend on the material's thermal
 252 conductivity λ . Temperature measurements allow us to identify these two
 253 parameters by minimizing $S = \sum_{t_d}^{t_f} (T_{\text{exp}}(t) - T_0(t))^2$ on a time interval $[t_d, t_f]$,

254 where T_{exp} is the experimental temperature measured by the thermocouple
255 and T_0 the temperature obtained from Eq. (25). The thermal conductivity
256 is finally obtained by evaluating the following equation:

$$\lambda = \frac{\phi}{4\pi D_2}. \quad (26)$$

257 At a given temperature, the experiments are repeated three times and the
258 final value of conductivity is taken as the mean of these experiments. The
259 maximum variation of λ obtained in this way is $0.02 \text{ W m}^{-1} \text{ K}^{-1}$.

260 *2.4. Specific heat capacity and latent heat*

261 The specific heat capacity c_p as well as the latent heat of the material are
262 obtained using a Setaram μdSc3 differential calorimeter.

263 The protocol consists in applying temperature variations to the sample
264 (sample mass about 200 - 300 mg) and in measuring simultaneously the
265 heat transfer over time. Here, temperature variations are generated either
266 through ramps of different rates of cooling/heating (1 K min^{-1} , 0.5 K min^{-1} ,
267 0.2 K min^{-1}) or through temperature steps that lead to quasi-steady thermal
268 conditions. In the latter case, steps last long enough to recover the steady
269 state, that is, until there is no more heat flux between the sample and the
270 device. In our experiments, this corresponds to a minimum of 1 hour up
271 to 2 hours per temperature step. Increments between temperature steps are
272 set to 1 K when phase change occurs, i.e. between 283.15 K and 303.15 K,
273 to gain accuracy in evaluating the effective $c_p(T)$. Outside this temperature
274 range, the increment is 2 K. The increment between two successive steps is
275 obtained by applying a temperature ramp of 0.2 K min^{-1} .

276 Long steps or slow temperature variations have the advantage to avoid
277 or at least to minimize undercooling effects [26]. Reversibility of results
278 are tested performing the entire protocol both increasing and decreasing the
279 temperature. The effective heat capacity is deduced from the heat transferred
280 to the sample after each temperature variation. At the phase transition, the
281 effective c_p varies strongly due to the addition of latent heat to sensible
282 heat. The latent heat is therefore estimated by subtracting the sensible heat
283 obtained for the liquid or solid phase from the total heat measured at the
284 phase change.

285 A method validation for our experimental conditions and post-process is
286 provided in the supplementary materials.

287 **3. Results**

288 *3.1. Density*

289 *3.1.1. Liquid phase*

290 Density measurements of PEG 600 are presented in Fig. 5 in the tem-
291 perature range of [294.15, 373.15] K. Measurements have been performed by
292 cooling the sample in order to avoid any issues related with the formation of
293 bubbles (that occurs when the material is heated over a large temperature
294 range) or with the presence of a mushy phase at the beginning of the analysis,
295 i.e. around 294.15 K. This precaution enables to obtain reproducible density
296 values under our experimental conditions.

297 Our experimental values are summarized in Fig. 5 together with values
298 currently present in literature [18, 15, 16]. We observe a very good agreement
299 between our results and literature (see also Table 3 where deviations are
300 shown). Our results are found within a maximum difference of 1% from
301 those reported in the above cited studies. Our results can be fitted by a
302 linear model (continuous line in Fig. 5) as follows:

$$\rho(T) = p_1 \times T + p_2 \quad (\text{g cm}^{-3}), \quad (27)$$

303 with $p_1 = -0.00081643 \text{ g cm}^{-3} \text{ K}^{-1}$, $p_2 = 1.3652 \text{ g cm}^{-3}$ and T the tempera-
304 ture in K. The intervals of the coefficients with 95% confidence bounds are
305 $p_1 = [-0.0008182, -0.0008147]$ and $p_2 = [1.365, 1.366]$.

306 Furthermore, the thermal expansion coefficient β can be evaluated ac-
307 cording to Eq. (1). For instance, at $P = 1.007 \text{ bar}$ and $T_{ref} = 298.15 \text{ K}$, we
308 obtain $\rho_{ref} = 1.121961 \text{ g cm}^{-3}$ and $\beta = 7.28 \times 10^{-4} \text{ K}^{-1}$, with an estimated
309 standard uncertainty of $u(\beta) = 0.02 \times 10^{-4} \text{ K}^{-1}$.

310 *3.1.2. Solid phase*

311 The density of PEG 600 in solid phase is obtained using the pycnometer
312 described in section 2.2.2. A material sample of about 150 g is placed in the
313 upper cavity of the pycnometer. The latter is left inside the thermostatic
314 chamber for 24 hours at temperature of 273.75 K. This is done before per-
315 forming any measurement in order to ensure the complete solidification of the
316 sample. Density measurements are afterward carried out at the same tem-
317 perature of 273.75 K by keeping the pycnometer with the solid sample inside
318 the thermostatic chamber for the entire duration of the experiment. Two
319 sets of pressure measurements are performed, in each of which the measure-
320 ment is repeated 4 times (see Table 4). After the first set of measurement,

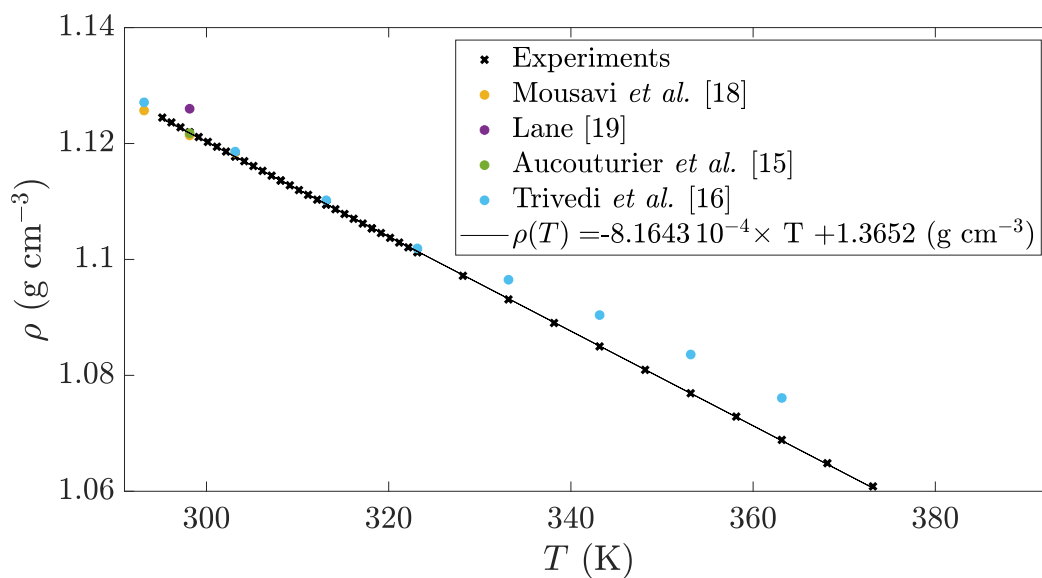


Figure 5: Density ρ of PEG 600 as a function of temperature T at the pressure $P=1.007$ bar. Data are provided in supporting files. Standard uncertainties u are $u(P)=0.018$ bar and $u(T) = 0.01$ K. The combined expanded uncertainty U_c is $U_c(\rho)=2\times 10^{-3}$ g cm $^{-3}$, with 0.95 level of confidence ($k=2$) and considering a contribution due to purity (x_e) of $u(x_e) = 0.002/\sqrt{3} = 0.0012$.

Table 3: Comparison between some of our density measurements (ρ) of PEG 600 with values given in literature (ρ_{lit}) at different temperatures T and pressure $P=1.007 \text{ bar}^a$.

T (K)	ρ (\times) (g cm^{-3})	ρ_{lit} (\circ) (g cm^{-3})	Reference	Deviation (%)
298.15	1.121961	1.126	[19]	0.36
		1.1214	[18]	0.05
		1.12177	[15]	0.02
303.15	1.117783	1.1184	[18]	0.06
		1.1186	[16]	0.07
313.15	1.109497	1.1102	[16]	0.06
323.15	1.101295	1.1019	[16]	0.06
333.15	1.093104	1.0965	[16]	0.31
343.15	1.084992	1.0904	[16]	0.50
353.15	1.076914	1.0836	[16]	0.62
363.15	1.068864	1.0761	[16]	0.67

Standard uncertainties u are $u(P)=0.018 \text{ bar}$ and $u(T) = 0.01 \text{ K}$. The combined expanded uncertainty U_c is $U_c(\rho)=2\times 10^{-3} \text{ g cm}^{-3}$, with 0.95 level of confidence ($k=2$) and considering a contribution due to purity (x_e) of $u(x_e) = 0.002/\sqrt{3} = 0.0012$.

321 the sample is removed from the device and melted. The protocol is then
 322 performed again for the second set.

323 For the range of PEG volume involved in our experiments, the error of
 324 measurements is found smaller than 5%. This value is obtained using a
 325 stainless steel sample with a known volume of $3.92 \times 10^{-5} \text{ m}^3$. The volume
 326 measured with the pycnometer led to $V_{\text{sample}} = 3.82 \times 10^{-5} \text{ m}^3$, i.e. within
 327 2.6 % difference with the real value.

328 The density of PEG 600 in solid phase and at 273.75 K is evaluated to
 329 $\rho = 1510 \text{ kg m}^{-3}$ with a standard uncertainty $u(\rho) = 23 \text{ kg m}^{-3}$. This value
 330 results to be quite different from the one obtained for the liquid phase. This
 331 is not surprising as it is correlated to the large variation in volume occurring
 332 during solidification.

333 3.2. Thermal conductivity

334 3.2.1. Liquid phase - Steady hot tube method

335 As above mentioned in section 2.3.1, the steady hot tube method is rel-
 336 evant only in the liquid phase as it requires good thermal contacts between
 337 sample and tubes surfaces. Since the device is filled with PEG 600 in liquid
 338 phase, the largest decrease in volume that leads to thermal resistances at

Table 4: Pressure measurements performed for one sample of PEG 600 at 273.75 K. ^a

First set			Second set		
P_i (bar)	P_f (bar)	P_f/P_i	P_i (bar)	P_f (bar)	P_f/P_i
3.317	1.816	54.7 %	3.555	1.943	54.6 %
3.266	1.788	54.7 %	3.365	1.851	54.7 %
3.415	1.869	54.7 %	3.296	1.807	55.0 %
3.548	1.938	54.6 %	3.399	1.861	54.8 %

^aStandard uncertainties u are $u(P) = 0.001$ bar and $u(T) = 0.01$ K.

339 interfaces is observed at the liquid-to-solid transition. At temperature below
 340 293.15 K results are indeed no longer reproducible. For higher temperatures,
 341 however, surface contact resistances can be assumed to be negligible. Mea-
 342 surements are performed at steady state. Results obtained with this device
 343 are presented in Fig. 6 ('+' symbols) as a function of the mean temperature
 344 between the two thermocouples, i.e. $\bar{T} = T = (T_1 + T_2)/2$. For comparison,
 345 additional values of thermal conductivity given by Lane [19] and values from
 346 a data sheet provided by Dynalene [30] are also displayed in Fig. 6. In our
 347 experiments the temperature variation $\Delta T = T_2 - T_1$ does not exceed 3 K
 348 through the annular region of the device, i.e. between r_1 and r_2 . In the range
 349 of the tested temperatures, we observe a slight temperature dependence of
 350 λ . These measurements are complemented by those obtained by using the
 351 hot needle method.

352 3.2.2. Solid and liquid phases - Hot needle method

353 The measurements are carried out with the needle probe described pre-
 354 viously in Section 2.3.2. The estimation of the thermal conductivity λ
 355 is obtained assuming: (i) conductive regime in the vicinity of the needle, (ii)
 356 an infinite medium and (iii) $T_0(t) \propto \ln(t)$ at long time. The time interval
 357 $[t_i, t_f]$, in which the latter condition is satisfied, is determined empirically
 358 when the difference between experiments and the model is close to zero (see
 359 the discussion below about residuals).

360 Thermal conductivity values in the solid phase are obtained placing the
 361 device in the temperature controlled binder. An example of temperature
 362 measurement ($T^* = T_0(t) - T_0(0)$) is plotted in Fig. 7 as a function of
 363 time. In the same figure we also display temperature values estimated by the
 364 model given by Eq. (25). Residuals multiplied by 10 times are also plotted in

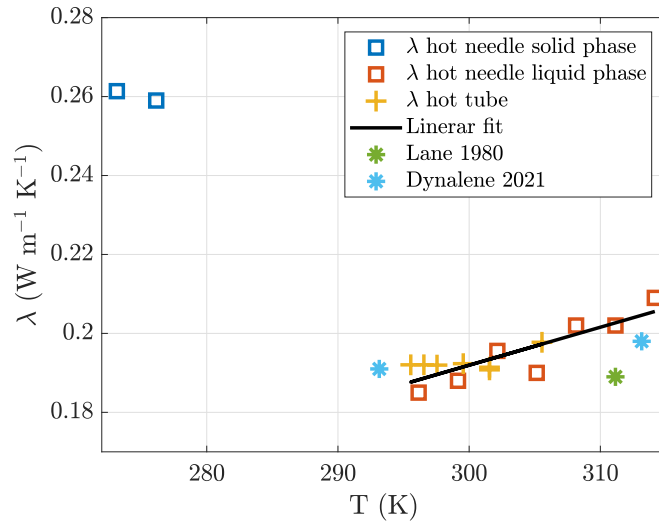


Figure 6: Thermal conductivity results for liquid phase and solid phases at the pressure $P=1.007$ bar. The temperature T refers (i) to the mean temperature between thermocouples $T = \bar{T} = (T_1 + T_2)/2$ in the case of the hot tube method and (ii) to the temperature in the thermostatic enclosure in the case of the hot needle method. Data are provided in supporting files. Standard uncertainties u are $u(P)=0.018$ bar and $u(T) = 0.1$ K. The combined expanded uncertainty U_c is $U_c(\lambda) = 0.04$ W m⁻¹ K⁻¹ with 0.95 level of confidence ($k \approx 2$), for both hot tube method and hot needle method.

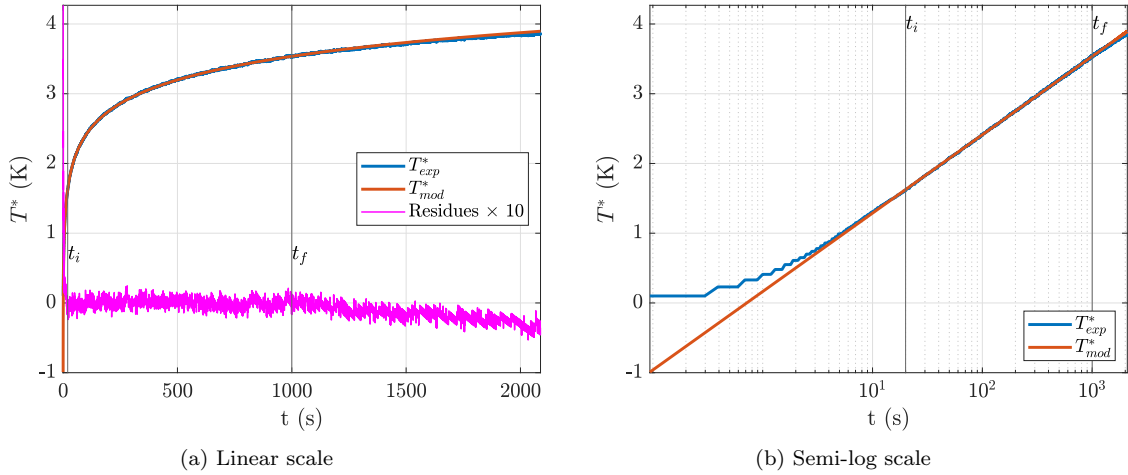


Figure 7: Time evolution of experimental (T_{exp}^* , in blue) and simulated (T_{mod}^* , in red) temperature difference T^* between the hot needle and the thermostatic enclosure set at 276.15 K and $P=1.007$ bar. The red curve is obtained with the simplified model from Eq. (25). Magenta curve in (a) displays the residues S between T_{exp} and T_{mod} multiplied by 10 times. Data are provided in supporting materials. Standard uncertainties u are $u(P)=0.018$ bar, $u(T^*)=0.02$ K and $u(t)=0.001$ s.

365 order to highlight the differences between measurements and the model. For
 366 each set of experiments, we determine the time interval $[t_i, t_f]$ along which
 367 residuals are perfectly flat and centered on zero, i.e. the time interval in
 368 which our model is consistent. This interval is bounded by vertical lines in
 369 Figs. 7 and 8. In the case presented in Fig. 7, the estimation time interval is
 370 $[20, 1000]$ s. The divergence of the residuals after 1000 s indicates the limit of
 371 validity of the infinite medium assumption. Following Eq. (25), we evaluate
 372 D_2 within the estimation interval as the slope of the temperature variation
 373 with time in semi-log scale (Fig. 7b).

374 The model also applies to the liquid phase only if convection does not
 375 occur. For this reason, we have also performed some measurements above
 376 293.15 K. We show them in Fig. 8, where experimental and simulated tem-
 377 perature variations are displayed as a function of time. The same conditions
 378 described above are assumed and residuals are again plotted multiplied by
 379 10 times. Figure 8 corresponds to two different temperatures imposed in the
 380 chamber, i.e. 299.15 K and 314.15 K. The estimation interval was adjusted
 381 to $[50, 300]$ s for the measurement at 299.15 K and to $[20, 60]$ s for the
 382 measurement at 314.15 K. The residuals are found flat and centered on zero

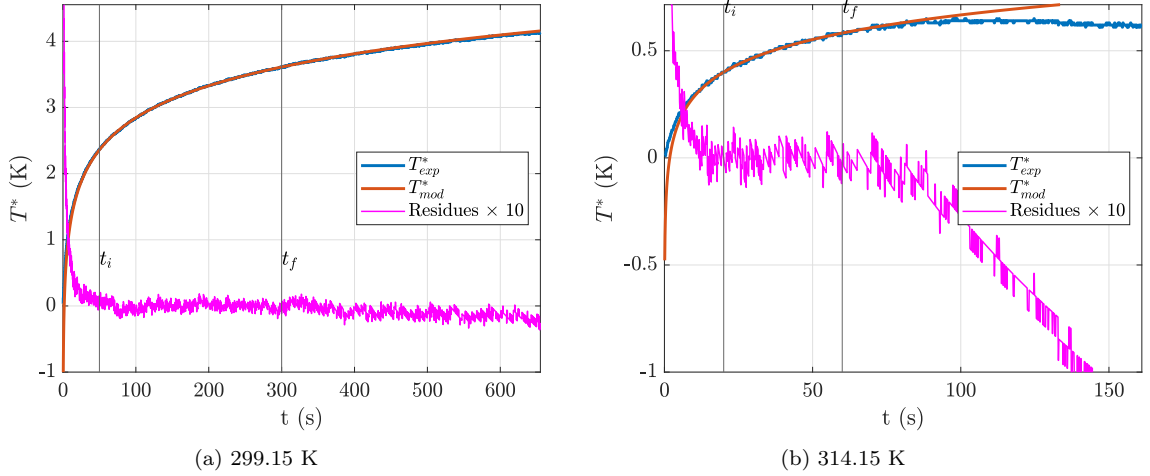


Figure 8: Time evolution of experimental (T_{exp}^* , in blue) and simulated (T_{mod}^* , in red) temperature difference T^* between the hot needle and the thermostatic enclosure set at $P=1.007$ bar and 299.15 K (a) and 314.15 K (b). The red curve is obtained with the simplified model from Eq. (25). Magenta curves display the residues between T_{exp}^* and T_{mod}^* multiplied by 10 times. Data are provided in supporting materials. Standard uncertainties u are $u(P)=0.018$ bar, $u(T^*)=0.02$ K and $u(t)=0.001$ s.

383 over these intervals. In the case of 314.15 K, the divergence of the residuals
 384 after 60 s is explained by the occurrence of convection around the needle.
 385 The higher the temperature is, the earlier this phenomenon appears. For
 386 instance, convection is not observed before 300 s for the case at 299.15 K.

387 Figure 6 summarizes all the thermal conductivity measurements as a function
 388 of temperature carried out for PEG 600. In liquid phase, values obtained
 389 via the needle method (square symbols) are consistent with those obtained
 390 using the hot tube method. As temperature increases, the thermal conductivity
 391 in the liquid phase shows a slight increase. This follows a linear variation
 392 in the form of $\lambda(T) = 9.61 \times 10^{-4} T - 9.66 \times 10^{-2}$, with λ in $\text{W m}^{-1} \text{K}^{-1}$
 393 and temperature T in K. The intervals of the coefficients with 95% confidence
 394 bounds are $p_1 = [0.0006076, 0.001316]$ and $p_2 = [-0.2037, 0.01055]$.

395 Our results are very close to those provided by Dynalene (see the data
 396 sheet in [30]), i.e. $\lambda = 0.191 \text{ W m}^{-1} \text{K}^{-1}$ at 293.15 K and $\lambda = 0.198$
 397 $\text{W m}^{-1} \text{K}^{-1}$ at 313.15 K. A good agreement is also found with values pub-
 398 lished by Lane [19], who obtained $\lambda = 0.189 \text{ W m}^{-1} \text{K}^{-1}$ at 311.00 K and
 399 $\lambda = 0.187 \text{ W m}^{-1} \text{K}^{-1}$ at 340.15 K.

400 In solid phase, the value of conductivity measured at 273.15 K and 276.15

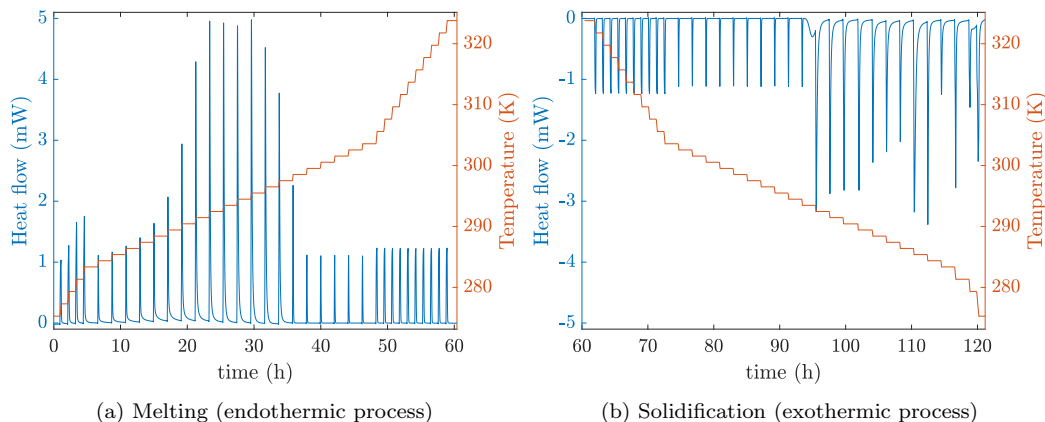


Figure 9: Heat flow rate measured from DSC (in blue) and imposed temperature steps (in red) as a function of time and at the pressure $P=1.007$ bar. (a) Melting of PEG 600 for increasing temperature steps (endothermic process). (b) Solidification of PEG 600 for decreasing temperature steps (exothermic process). Data are provided in supporting files. Standard uncertainties u are $u(P)=0.018$ bar, $u(\text{Heat flow})=0.01$ mW and $u(T)=0.01$ K.

401 K does not vary much, leading for this temperature interval to $\lambda_s \approx 0.260$
 402 $\text{W m}^{-1} \text{K}^{-1}$, with a standard uncertainty of $u(\lambda)=0.02 \text{ W m}^{-1} \text{K}^{-1}$. This
 403 value is close to the one proposed by Kou et al [14] for PEG 1000, i.e.
 404 $0.29 \pm 0.05 \text{ W m}^{-1} \text{K}^{-1}$. In our experiments, for an enclosure temperature
 405 of 279.15 K, the temperature near the needle is around 283.00 K and the
 406 material starts to melt. This makes it difficult to obtain values of λ of PEG
 407 600 in solid phase above 276.15 K. The gap between 276.15 K and 293.15 K
 408 in terms of thermal conductivity (Fig. 6) is explained by the occurrence of
 409 the phase transition.

410 To summarize, our measurements provide values of thermal conductivity
 411 in both liquid and solid phases. An effective value of λ in solid phase can
 412 be measured in the temperature range [276.15, 293.15] K. However, we think
 413 that a careful investigation of the material structure at the phase transition
 414 would be more relevant. This aspect is beyond the scope of this article but
 415 it will be investigated in the near future.

416 3.3. Specific heat capacity and latent heat

417 Raw data obtained by differential scanning calorimetry are presented in
 418 Fig. 9. The figure displays the amount of heat flux (in blue) transferred

419 between the PCM sample and the calorimeter, for the case of imposed tem-
 420 perature steps (in red). Each increment of temperature leads to a peak in
 421 terms of heat exchanged. The latter goes back to zero as soon as the thermal
 422 equilibrium is reached. Given this experimental protocol, the effective heat
 423 capacity c_p is deduced by integrating the heat flux over the duration of a step
 424 (including the increment) and dividing the result by the mass of the sample
 425 m and the temperature increment.

426 On the other hand, when the protocol involves temperature ramps, i.e.
 427 continuous temperature variations with time, we directly determine the ef-
 428 fective c_p from the measured heat flux ϕ according to

$$\phi = mc_p \frac{dT}{dt}, \quad (28)$$

429 where the temperature variation rate $\frac{dT}{dt}$ is constant and imposed by the
 430 ramp. We deduce then:

$$c_p = \frac{\phi}{m} \left(\frac{dT}{dt} \right)^{-1}. \quad (29)$$

431 The resulting values of effective c_p are shown in Fig. 10 as a function
 432 of temperature. Similar trends are observed for all tested protocols. When
 433 the material is liquid, i.e. for large temperature values (above 298.15 K) and
 434 at pressure $P=1.007 \pm 0.018$ bar, we obtain a quasi constant heat capacity,
 435 i.e. $c_p = 2.13 \text{ kJ kg}^{-1} \text{ K}^{-1}$, corresponding to $1278 \text{ J K}^{-1} \text{ mol}^{-1}$. The standard
 436 uncertainty for c_p is $0.06 \text{ kJ kg}^{-1} \text{ K}^{-1}$. This value of heat capacity is recovered
 437 in the liquid phase for both cooling and heating experiments.

438 Similarly, when the material is solid, i.e. for low temperature values (be-
 439 tween 275.15 K and 267.15 K) and $P=1.007 \pm 0.018$ bar, we obtain $c_p = 4.3$
 440 $\text{kJ kg}^{-1} \text{ K}^{-1}$, corresponding to $2580 \text{ J K}^{-1} \text{ mol}^{-1}$, with a standard uncertainty
 441 $u(c_p)=0.3 \text{ kJ kg}^{-1} \text{ K}^{-1}$. This value of c_p has been obtained performing tem-
 442 perature steps of 2 hours with an increment of 2 K between two steps. Results
 443 lead to a constant value of c_p whether heating or cooling the PEG sample.

444 In the temperature range where the phase transition occurs (i.e. solidifi-
 445 cation in Fig. 10a and melting in Fig. 10b), variations in the evaluated c_p
 446 are due to the competition between the kinetics of the phase change process
 447 and the rate of temperature variations. This competition leads to a tempera-
 448 ture hysteresis during solidification that corresponds to undercooling effects.
 449 This latter phenomena decreases for slow temperature variations. In the case

450 of imposed temperature steps, the melting of PEG 600 is observed between
451 283.4 K and 298.5 K, while its solidification occurs between 294.5 K and
452 281.3 K. Further differences between melting and freezing processes can be
453 highlighted. Indeed, two distinct local maxima are observed during solidifi-
454 cation as the temperature decreases (Fig. 10a). These extrema are always
455 obtained for similar temperature values when the adopted cooling protocol
456 lasts long enough. Here, extrema correspond to exothermal transformations
457 correlated to structural modifications that occur during the crystallization
458 [20, 21].

459 Reciprocally, at least one extremum value in terms of c_p is also obtained
460 for the melting process (Fig. 10b). When the heating process is long enough
461 (0.2 K min^{-1}), two local peaks are observed but their amplitudes are smaller
462 than in the case of the solidification process. These multiple peaks are ob-
463 served also in other studies where they are attributed to microstructural
464 variations, i.e. crystals with different thickness due to variations in folds
465 number in the polymer chain [31] or due to the evolution of the lamellar
466 microstructure during the phase change [32].

467 A comparison of the effective c_p obtained for PEG 600 with PEGs with
468 higher molar masses [14] is proposed in Fig. 11. All results are obtained
469 during the melting process and by heating samples with a rate of 1 K min^{-1}
470 for PEG 600 and a rate of 10 K min^{-1} [14] for PEG with large molar masses
471 (from 1000 to 20000). Our data for PEG 600 follow similar tendencies to
472 those observed by [14] as the average molar mass of PEG increases, i.e. both
473 melting temperature and c_p increase.

474 Finally, the latent heat is evaluated by integrating only the part due to the
475 phase transition in the effective heat capacity. For the solidification process,
476 the integration leads to a latent heat of 128.0 kJ kg^{-1} , while for the melting
477 to 128.7 kJ kg^{-1} . In both cases, we estimate a standard uncertainty for the
478 latent heat of 2 kJ kg^{-1} . These values are in very good agreement with the
479 one proposed by Lane [19], i.e. 127.2 kJ kg^{-1} . According to Pielichowski
480 & Flejtuch [33], the latent heat of melting of a 100% crystalline polymer is
481 196.8 kJ kg^{-1} . Compared with this latter value, PEG 600 should correspond
482 to a degree of crystallinity of 65%. Indeed, low molecular weight polymers
483 are known to have higher segmental mobility, thus reducing the formation of
484 the crystalline phase (geometric alignment), as observed for PEG at different
485 molecular weight [14, 33].

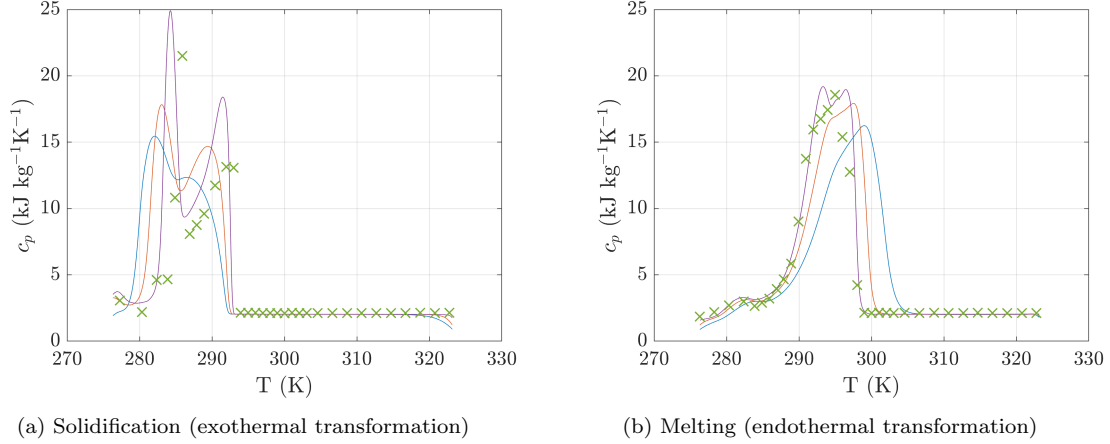


Figure 10: Effective $c_p(T)$ evaluated at constant pressure $P=1.007$ bar and during (a) the solidification process and (b) the melting process, for temperature variations of 1 K min^{-1} (blue lines), 0.5 K min^{-1} (red lines), 0.2 K min^{-1} (purple lines) and temperature steps (green crosses). Data are provided in supporting materials. Standard uncertainties u are $u(P)=0.018$ bar, $u(\text{Heat flow})=0.01$ mW, $u(T)=0.01$ K, $u(m)=0.01$ mg and $u(c_p)=0.06 \text{ kJ kg}^{-1} \text{ K}^{-1}$.

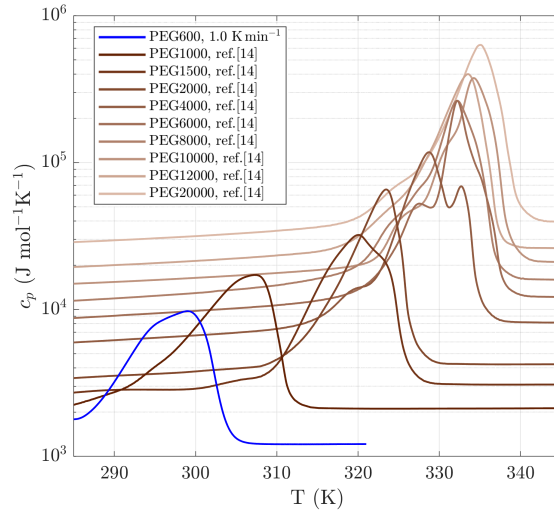


Figure 11: Comparison between the effective $c_p(T)$ for PEG 600 (blue line) and data of [14] for PEG with large molar masses (brown lines). In both cases, the curves are obtained from DSC measurements during the melting process. For a better comparison, heat capacity is plotted in $\text{J mol}^{-1} \text{ K}^{-1}$. For PEG 600 we display the same curve shown in Fig. 10b for a heating rate of 1.0 K min^{-1} . Uncertainties are those reported in Fig. 10b.

486 4. Conclusion

487 In this study we report the thermal properties of polyethylene glycol 600
488 (PEG 600). The density in liquid phase has been measured in the tempera-
489 ture range [298.15, 373.15] K. Given the small temperature increments used,
490 we have been able to provide a fit for the temperature-dependent density of
491 liquid PEG 600. The latter allows to determine the coefficient of thermal vol-
492 ume expansion with a good accuracy. The density of PEG 600 in solid phase
493 has been measured by using a pycnometer and it results in $\rho = 1510 \text{ kg m}^{-3}$
494 with a standard uncertainty $u(\rho) = 23 \text{ kg m}^{-3}$ at 273.75 K. The variation
495 of density between the two phases highlights a quite large volume shrinkage
496 of the material during solidification. This can have a drastic consequence on
497 thermal contacts at interfaces and hence a strong impact in the usability of
498 this PCM in thermal energy storage systems.

499 The thermal conductivity λ has been investigated with two different meth-
500 ods. Results for the liquid phase show a slight linear increase of λ with in-
501 creasing temperature. For the solid phase, and within the investigated tem-
502 perature range, we find $\lambda \approx 0.260 \text{ W m}^{-1} \text{ K}^{-1}$ with a standard uncertainty
503 of $u(\lambda) = 0.02 \text{ W m}^{-1} \text{ K}^{-1}$.

504 Effective heat capacity and heat transfer have been described and quan-
505 tified by DSC measurements. Far from the phase transition, we obtain a
506 constant specific heat capacity for both solid and liquid phase. Whether
507 the sample is slowly cooled or heated, the phase transition starts at 283.4 K
508 and at 294.5 K for the melting and solidification process, respectively. Under-
509 cooling effects are responsible for the hysteresis in phase change temperature,
510 however they decrease when the cooling rate is decreased. DSC experiments
511 enable us to obtain a latent heat of about 128.0 kJ kg^{-1} , which is close to the
512 value proposed by Lane [19]. Furthermore, during the solidification process
513 we observe several exothermic heat flow peaks that highlight consecutive re-
514 organizations of aggregates and/or crystals in the internal structure of PEG
515 600. This latter aspect is beyond the scope of this study. However, since
516 explanations on PEG crystallization are still controversial in literature, a
517 proper investigation at small scales of this process will be a fundamental
518 part of our future work.

519 **Appendix A. Estimation of the error due to steady-state contact**
 520 **resistances**

521 During solidification, the density of the sample increases and $\rho_l < \rho_s$, with
 522 ρ_l being the density of the liquid phase and ρ_s the one of the solid phase.
 523 This results in a decrease in volume with temperature. In the hot tube device
 524 used to measure the thermal conductivity, this leads to an air/vacuum layer
 525 of thickness ϵ between the sample and the inner heating tube of radius r_1
 526 (Fig. 2).

527 One can write:

$$\rho_l \pi (r_2^2 - r_1^2) = \rho_s \pi [r_2^2 - (r_1 + \epsilon)^2], \quad (\text{A.1})$$

leading to

$$\epsilon = \left[r_2^2 - \frac{\rho_l}{\rho_s} (r_2^2 - r_1^2) \right]^{0.5} - r_1.$$

528 The thermal resistance between the two tubes is:

$$R = \frac{1}{2\pi\lambda} \ln \left(\frac{r_2}{r_2 - r_1 - \epsilon} \right) + \frac{1}{2\pi\lambda_{air}} \ln \left(\frac{r_1 + \epsilon}{r_1} \right) = \frac{1}{2\pi\lambda_m} \ln \left(\frac{r_2}{r_1} \right). \quad (\text{A.2})$$

529 In this way, λ_m is the measured value of the thermal conductivity while
 530 λ is the real thermal conductivity of the solid sample. We deduce:

$$\lambda_m = \ln \left(\frac{r_2}{r_1} \right) \left[\frac{1}{\lambda} \ln \left(\frac{r_2}{r_2 - r_1 - \epsilon} \right) + \frac{1}{\lambda_{air}} \ln \left(\frac{r_1 + \epsilon}{r_1} \right) \right]^{-1}. \quad (\text{A.3})$$

531 The radii values are $r_1 = 2.75$ mm; $r_2 = 6$ mm. With an estimated
 532 value for the thermal conductivity in solid phase of $\lambda = 0.26$ W m⁻¹ K⁻¹, we
 533 can calculate the value λ_m that we would have measured with the hot tube
 534 method. For $\rho_l/\rho_s = 0.75$, the calculation leads to $\lambda_m = 0.19$ W m⁻¹ K⁻¹, i.e.
 535 around 30% less than the actual value. For this reason, the steady-state hot
 536 tube device used in this study to measure λ of liquid PEG 600 is unsuitable
 537 to retrieve λ of the solid phase. For measurements of thermal conductivity
 538 of solid PCMs is therefore preferable to use a transient measurement device
 539 where contact resistances have no influence on estimating the conductivity.

540 **Acknowledgments**

541 Financial supports have been brought to this work by the operation
542 “STOCK’NRJ” co-financed by the European Union within the framework
543 of the Program FEDER-FSE Lorraine and Massif des Vosges 2014-2020.
544 This work is part of the ”CONVINCES” project financially supported by
545 the French National Research Agency (ANR).

546 **References**

- 547 [1] M. Kobayashi, T. Koide, S.-H. Hyon, Tribological characteristics of
548 polyethylene glycol (PEG) as a lubricant for wear resistance of ultra-
549 high-molecular-weight polyethylene (UHMWPE) in artificial knee joint,
550 *Journal of the Mechanical Behavior of Biomedical Materials* 38 (2014)
551 33–38.
- 552 [2] K. Bjugstad, D. Redmond Jr, K. Lampe, D. Kern, J. Sladek Jr, M. Ma-
553 honey, Biocompatibility of PEG-based hydrogels in primate brain, *Cell*
554 *Transplantation* 17 (4) (2008) 409–415.
- 555 [3] A. K. Jain, A. K. Goyal, N. Mishra, B. Vaidya, S. Mangal, S. P. Vyas,
556 PEG–PLA–PEG block copolymeric nanoparticles for oral immunization
557 against hepatitis B, *International Journal of Pharmaceutics* 387 (1-2)
558 (2010) 253–262.
- 559 [4] S. M. Baygi, S. Sadrameli, Thermal management of photovoltaic so-
560 lar cells using polyethylene glycol 1000 (PEG1000) as a phase change
561 material, *Thermal Science and Engineering Progress* 5 (2018) 405–411.
- 562 [5] F. Hamad, E. Egelle, K. Cummings, P. Russell, Investigation of the
563 melting process of polyethylene glycol 1500 (PEG 1500) in a rectangular
564 enclosure, *International Journal of Heat and Mass Transfer* 114 (2017)
565 1234–1247.
- 566 [6] J. Wang, M. Yang, Y. Lu, Z. Jin, L. Tan, H. Gao, S. Fan, W. Dong,
567 G. Wang, Surface functionalization engineering driven crystallization
568 behavior of polyethylene glycol confined in mesoporous silica for shape-
569 stabilized phase change materials, *Nano Energy* 19 (2016) 78–87.

- 570 [7] J. Yang, E. Zhang, X. Li, Y. Zhang, J. Qu, Z.-Z. Yu, Cellulose/graphene
571 aerogel supported phase change composites with high thermal conduc-
572 tivity and good shape stability for thermal energy storage, *Carbon* 98
573 (2016) 50–57.
- 574 [8] J. Jin, F. Lin, R. Liu, T. Xiao, J. Zheng, G. Qian, H. Liu, P. Wen,
575 Preparation and thermal properties of mineral-supported polyethylene
576 glycol as form-stable composite phase change materials (CPCMs) used
577 in asphalt pavements, *Scientific Reports* 7 (1) (2017) 1–10.
- 578 [9] Y. Zhou, X. Liu, D. Sheng, C. Lin, F. Ji, L. Dong, S. Xu, H. Wu,
579 Y. Yang, Graphene oxide/polyurethane-based solid–solid phase change
580 materials with enhanced mechanical properties, *Thermochimica Acta*
581 658 (2017) 38–46.
- 582 [10] A. Sharma, V. V. Tyagi, C. Chen, D. Buddhi, Review on thermal energy
583 storage with phase change materials and applications, *Renewable and*
584 *Sustainable Energy Reviews* 13 (2) (2009) 318–345.
- 585 [11] B. Zalba, J. M. Marin, L. F. Cabeza, H. Mehling, Review on thermal
586 energy storage with phase change: materials, heat transfer analysis and
587 applications, *Applied Thermal Engineering* 23 (3) (2003) 251–283.
- 588 [12] M. Firoozzadeh, A. H. Shiravi, M. Shafiee, Experimental and ana-
589 lytical study on enhancing efficiency of the photovoltaic panels us-
590 ing Polyethylene-Glycol 600 (PEG 600) as a phase change mate-
591 rial, *Iranian Journal of Energy and Environment* 10 (2019) 23–32.
592 doi:10.5829/ijee.2019.10.01.04.
- 593 [13] R. Velraj, R. Seeniraj, B. Hafner, C. Faber, K. Schwarzer, Heat transfer
594 enhancement in a latent heat storage system, *Solar Energy* 65 (3) (1999)
595 171–180.
- 596 [14] Y. Kou, S. Wang, J. Luo, K. Sun, J. Zhang, Z. Tan, Q. Shi, Thermal
597 analysis and heat capacity study of polyethylene glycol (PEG) phase
598 change materials for thermal energy storage applications, *The Journal*
599 *of Chemical Thermodynamics* 128 (2019) 259–274.
- 600 [15] C. Aucouturier, G. Roux-Desgranges, A. Roux, Excess molar volumes
601 and excess molar heat capacities of (polyethylene glycols+ water) at

- 602 temperatures between $T=278$ K and $T=328$ K, The Journal of Chemical
603 Thermodynamics 31 (2) (1999) 289–300.
- 604 [16] S. Trivedi, C. Bhanot, S. Pandey, Densities of poly(ethylene glycol)+
605 water over the temperature range (283.15 to 363.15) K, The Journal of
606 Chemical Thermodynamics 42 (11) (2010) 1367–1371.
- 607 [17] A. Singh, R. Walvekar, M. Khalid, W. Y. Wong, T. Gupta, Thermo-
608 physical properties of glycerol and polyethylene glycol (PEG 600) based
609 DES, Journal of Molecular Liquids 252 (2018) 439–444.
- 610 [18] Z. Mousavi, M. Pirdashti, A. A. Rostami, E.-N. Dragoi, Thermophysical
611 properties analysis of poly (ethylene glycol) 600+ methanol, ethanol, 1-
612 propanol, and 2-propanol binary liquid mixtures, International Journal
613 of Thermophysics 41 (2) (2020) 1–26.
- 614 [19] G. A. Lane, Low temperature heat storage with phase change materials,
615 International Journal of Ambient Energy 1 (3) (1980) 155–168.
- 616 [20] L. Yang, T. Smith, Melting and solidification behavior of blends of high
617 density polyethylene with poly (butylene terephthalate), Polymer Engi-
618 neering & Science 33 (21) (1993) 1426–1430.
- 619 [21] A. Azri, P. Giamarchi, Y. Grohens, R. Olier, M. Privat, Polyethylene
620 glycol aggregates in water formed through hydrophobic helical struc-
621 tures, Journal of Colloid and Interface Science 379 (1) (2012) 14–19.
- 622 [22] B. Bogdanov, A. Vidts, E. Schacht, H. Berghmans, Isothermal crys-
623 tallization of poly (ϵ -caprolactone- ethylene glycol) block copolymers,
624 Macromolecules 32 (3) (1999) 726–731.
- 625 [23] K. Pielichowski, K. Flejtuch, Differential scanning calorimetry studies
626 on poly (ethylene glycol) with different molecular weights for thermal
627 energy storage materials, Polymers for Advanced Technologies 13 (10-
628 12) (2002) 690–696.
- 629 [24] D. D. Gray, A. Giorgini, The validity of the Boussinesq approximation
630 for liquids and gases, International Journal of Heat and Mass Transfer
631 19 (5) (1976) 545–551.

- 632 [25] Y. Jannot, A. Degiovanni, Thermal properties measurement of materi-
633 als, John Wiley & Sons, 2018.
- 634 [26] N. R. Sgreva, J. Noel, C. Metivier, P. Marchal, H. Chaynes, M. Isaiev,
635 Y. Jannot, Thermo-physical characterization of hexadecane during the
636 solid/liquid phase change, *Thermochimica Acta* (2022) 179 – 180.
- 637 [27] J. Huetz, J.-P. Petit, Notions de transfert thermique par convection,
638 *Techniques de l'Ingénieur* (A1504A) (Aug. 1990).
- 639 [28] M. L. V. Ramires, C. A. Nieto de Castro, Y. Nagasaka, A. Nagashima,
640 M. J. Assael, W. A. Wakeham, Standard reference data for the thermal
641 conductivity of water (1994).
- 642 [29] D. Maillet, S. Andre, J. C. Batsale, A. Degiovanni, C. Moyne, Ther-
643 mal quadrupoles: solving the heat equation through integral transforms,
644 Wiley-Blackwell, 2000.
- 645 [30] Dynalene Inc., PEG Series: Techincal data sheet,
646 [https://www.dynalene.com/product-category/heat-transfer-](https://www.dynalene.com/product-category/heat-transfer-fluids/polyethylene-glycol-heat-transfer-fluids/)
647 [fluids/polyethylene-glycol-heat-transfer-fluids/](https://www.dynalene.com/product-category/heat-transfer-fluids/polyethylene-glycol-heat-transfer-fluids/).
- 648 [31] B. Wunderlich, *Macromolecular physics: Crystal nucleation, Growth,*
649 *Annealing 2* (1976).
- 650 [32] M. S. Lisowski, Q. Liu, J. Cho, J. Runt, F. Yeh, B. S. Hsiao, Crystalliza-
651 tion behavior of poly (ethylene oxide) and its blends using time-resolved
652 wide-and small-angle X-ray scattering, *Macromolecules* 33 (13) (2000)
653 4842–4849.
- 654 [33] K. Pielichowski, K. Flejtuch, Differential scanning calorimetry studies
655 on poly (ethylene glycol) with different molecular weights for thermal
656 energy storage materials, *Polymers for Advanced Technologies* 13 (10-
657 12) (2002) 690–696.